SCIENCE CHINA Materials

ARTICLES

mater.scichina.com link.springer.com

Published online 4 March 2019 | https://doi.org/10.1007/s40843-018-9404-4

Unraveling the mechanochemical synthesis and luminescence in Mn^{II}-based two-dimensional hybrid perovskite $(C_4H_9NH_3)_2PbCl_4$

Guojun Zhou[1], Shaoqiang Guo[2], Jing Zhao[1], Maxim Molokeev[3,4,5], Quanlin Liu[1], Junying Zhang[2*] and Zhiguo Xia[1*]

ABSTRACT **The mechanochemical route is a facile and fast way and has received much attention for developing versatile advanced functional materials. Herein, we reported a mechanochemical synthesis for incorporating divalent manganese ions (Mn^{II}) into a two-dimensional (2D) hybrid perovskite $(C_4H_9NH_3)_2PbCl_4$. The mild external stimuli originating from the grinding at room temperature enabled the formation of Mn^{II}-doped 2D hybrid perovskites, and rapidly changed the luminescence characteristics. The photoluminescence analyses show that the violet and orange emissions are attributed to $(C_4H_9NH_3)_2Pb_{1-x}Mn_xCl_4$ band-edge emission and the $T_1 \rightarrow {}^6A_1$ transition of Mn^{2+} resulting from an efficient energy transfer process, respectively. Site preference and distribution of the doped Mn^{2+} cations on the locations of Pb^{2+} were analyzed. The formation energy calculated by the density functional theory (DFT) indicates that the Mn^{2+} ions can rapidly enter the crystal lattice due to the unique 2D crystal structure of the hybrid perovskite. Such a case of mechanochemical synthesis for the 2D hybrid perovskite motivates many novel emerging materials and the related applications.**

Keywords: 2D hybrid perovskite, mechanochemical, Mn-doping, luminescence, phosphor

INTRODUCTION

Two-dimensional (2D) organic–inorganic hybrid halide perovskites have been an important class of high-performance semiconductors and received significant attention in recent years due to their impressive structural diversity and the enormous potential in the fields like solar cells, photodetectors, lasers and light-emitting diodes [1–8]. Among hybrid semiconductors, the 2D layered hybrid perovskite quantum well materials $(C_nH_{2n+1}NH_3)_2(CH_3NH_3)_{m-1}Pb_mX_{3m+1}$, (X=Cl, Br, I; m=1, 2...; n=1, 2...) have attracted extensive attention, because the well width and the barrier width can be changed by altering m and n, respectively [9–12]. This layered structure is packed by one or more sheets of corner-shared PbX_6 octahedra and bilayers of organic cations alternating along the c axis [3]. The excitons within the octahedral planes are isolated by the organic layers which act as a dielectric spacer forming confining layers, leading to high oscillator strengths, high exciton binding energies, and fast radiative decay rates [8,9,13,14]. These features are highly beneficial to the applications in the field of lighting and displays. Here we aimed to determine the luminescent properties of 2D hybrid perovskites $(C_4H_9NH_3)_2PbCl_4$ (m=1, n=4). Up to now, the analogous series have been extensively explored for solar cells and photodetectors [7,8,15–16]. Despite some research on the intrinsic optical performance of 2D perovskites, such as $(C_6H_{11}NH_3)_2PbBr_4$ [17], $(C_6H_{13}N_3)PbBr_4$ [18], $(CH_3CH_2NH_3)_4Pb_3Br_{10-x}Cl_x$ [12], and others [1,9,13,19], little attention has been paid to the luminescence properties of 2D layered hybrid perovskite doped with

[1] Beijing Municipal Key Laboratory of New Energy Materials and Technologies, School of Materials Sciences and Engineering, University of Science and Technology Beijing, Beijing 100083, China
[2] Key Laboratory of Micro-nano Measurement, Manipulation and Physics (Ministry of Education), School of Physics, Beihang University, Beijing 100191, China
[3] Laboratory of Crystal Physics, Kirensky Institute of Physics, Federal Research Center KSC SB RAS, Krasnoyarsk 660036, Russia
[4] Siberian Federal University, Krasnoyarsk 660041, Russia
[5] Department of Physics, Far Eastern State Transport University, Khabarovsk 680021, Russia
* Corresponding authors (emails: zjy@buaa.edu.cn (Zhang J); xiazg@ustb.edu.cn (Xia Z))

transition metal ions (i.e., Mn^{2+}, Ni^{2+}, Co^{2+}) [14]. Doping Mn^{2+} ions in low-dimensional semiconductor materials in quantum confinement regime provides fascinating optical properties, due to the interaction of the quantum confined charge carriers of the host with the dopant ions [20–22]. Herein, we attempted to use $(C_4H_9NH_3)_2PbCl_4$-based bulk 2D layered perovskites as the active semiconductor host with incorporating Mn^{2+} dopant ions for energy transfer. Interestingly, the luminescent characteristics of Mn^{2+} were rapidly generated by only some mild external stimulus, such as room-temperature grinding, in Mn^{II}-based 2D chloride perovskites. The result shows that we developed a facile and effective mechanochemical synthesis for incorporating manganese ions into 2D organic-inorganic hybrid lead-halide perovskites. Nowadays, the mechanochemical synthesis has been considered to be a candidate for such a purpose, because high yields may be achieved in short times, without solvents, and generating small amounts of residuals [23]. This is an efficient and environment-friendly method that has been intensively studied [24,25]. Our strategy opens up a new way to achieving high-performance fluorescence based on the facile incorporation of the luminescent activators in the pre-synthesized hosts.

Therefore, considering the intriguing luminescence in Mn^{II}-based 2D hybrid perovskites, $(C_4H_9NH_3)_2PbCl_4$ is designed and measured by powder X-ray diffraction (PXRD) structural refinement, microstructure observation and elemental analysis, fluorescence analysis, UV-visible absorbance/reflection and the density functional theory (DFT) calculation. As expected, they exhibit quickly violet and orange emissions only by the mild grinding stimuli which are ascribed to $(C_4H_9NH_3)_2Pb_{1-x}Mn_xCl_4$ band-edge emission and the Mn^{2+}-based d–d transition ($^4T_1 \rightarrow {}^6A_1$) due to the exciton-to-$Mn^{2+}$ energy transfer, respectively. Meanwhile, the formation energies of the different phases were calculated and compared to take a deep insight into the essence of this phenomenon to further ascertain the validity of experiments. This fluorescence through mechanochemical synthesis shows potential applications in mechano-sensors, optical recording devices or fluorescent biomarkers.

EXPERIMENTAL SECTION

Materials and synthesis

$PbCl_2$ (99.9%, Aladdin), $MnBr_2{\cdot}5H_2O$ (99.5%, Sinopharm), $C_4H_9NH_2$ (*n*-butylamine 99.9%, Aladdin), C_7H_8 (toluene 99.5%, Sinopharm), $C_4H_{10}O$ (diethyl ether 99.7%, Sinopharm), CH_3OH (methanol 99.8%, Sinopharm), C_3H_6O (acetone 99.5%, Sinopharm), HCl (33% in water by weight, Sinopharm), *N*,*N*'-dimethylformamide (DMF 99.5%, Aladdin). All chemicals were used as received.

Precursor $C_4H_9NH_3Cl$: *n*-Butylamine (10 mL) was added into 25 mL methanol in a 100-mL 3-neck flask, and maintained at 0°C, using an ice-water bath. An appropriate amount of HCl aqueous solution (HCl: 13 mL, 33 wt%) was added dropwise to the above solution under vigorous stirring. Then the mixture was stirred at room temperature (RT) for about 3 h. The solution was then heated at about 70°C until all the methanol and water in the solution were removed. Here a white-solid product was washed repeatedly with ethyl ether, and after filtration the white solid was dried at 60°C for 24 h in a vacuum oven.

Synthesis of $(C_4H_9NH_3)_2PbCl_4$: The as-prepared $C_4H_9NH_3Cl$ (2 mmol) and $PbCl_2$ (1 mmol) were dissolved into 2 mL DMF and heated to 90°C. Toluene was added to the hot clear solution until the solution began to become cloudy. The heat was removed and the solution was naturally cooled to RT. This leads to the formation of lamellar white crystals in copious amounts. After standing for 5 h, the supernatant was removed and the crystals were washed repeatedly with acetone or diethyl ether. The $(C_4H_9NH_3)_2PbCl_4$ crystal was filtered and dried under vacuum at 60°C for 12 h.

Synthesis of $(C_4H_9NH_3)_2Pb_{1-x}Mn_xCl_4$: $MnBr_2{\cdot}5H_2O$ was used as the Mn^{2+} source, and preheated to remove the crystal water at 120°C. A desired amount of the above $(C_4H_9NH_3)_2PbCl_4$ was mixed with $MnBr_2$ (the amount of Mn salt added was decided by the relative mole percent of Pb) in an agate mortar. The powder was thoroughly ground for several minutes and used for the further characterizations.

Characterization

The PXRD data were collected by using a D8 Advance diffractometer (Bruker Corporation, Germany) at 40 kV and 40 mA with monochromatized Cu Kα radiation (λ=1.5406 Å). The scanning rate for phase identification was fixed at 8° min^{-1} with a 2θ range from 5° to 50°, and the data for Rietveld analysis was collected in a step-scanning mode with a step size of 0.02° and 5 s counting time per step over a 2θ range from 5° to 120°. Rietveld refinements were performed by using TOPAS 4.2 software.

The morphology observation was conducted by a

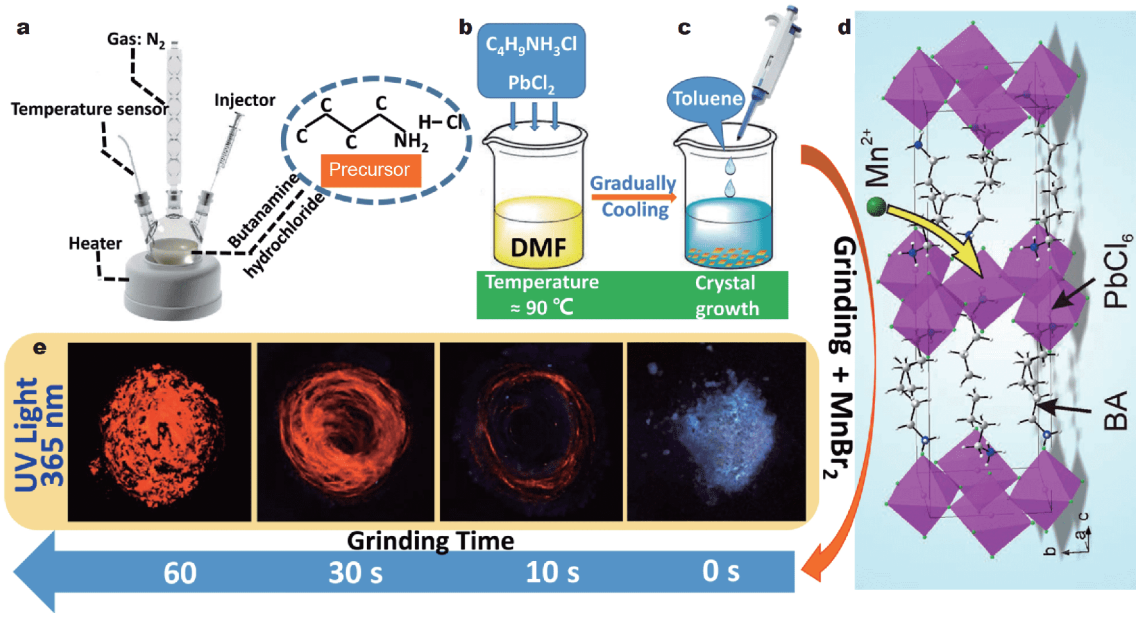

Figure 1 (a–c) Illustrations of the three-step synthesis process including the precursor synthesis (a), self-assembly (b) and crystallization (c), and the crystallization method is related with the crystal quality of the targeted product. (d) Crystal structure of the 2D layered hybrid perovskite derived from the 3D $APbX_3$ lattice along the <100> direction, and the interlayer catenoid organic ligand plays a key role in the formation of layered perovskite. (e) Grinding time dependent fluorescence images in Mn^{II}-based 2D hybrid perovskite, showing that the luminescent characteristics of Mn^{2+} can be rapidly generated only by grinding at RT.

scanning electron microscope (SEM, JEOL JSM-6510) and the elemental composition was determined using energy dispersive X-ray spectroscopy (EDS) that was attached to the SEM. Transmission electron microscopy (TEM) was performed on a JEM-2010 operated at 120 keV on 200 mesh carbon coated nickel grids and EDS was performed on a probe aberration corrected microscope, JEOL JEM-ARM200CF, at 200 kV.

The room-temperature photoluminescence (PL), photoluminescence excitation (PLE) spectra and luminescence decay curves were carried out using a FLSP9200 fluorescence spectrophotometer (Edinburgh Instruments Ltd., U. K.). The absorption spectra were measured on a UV-vis-NIR spectrophotometer (SolidSpec-3700 Shimadzu) with $BaSO_4$ serving as the reference standard. The photoluminescence quantum yields (PLQYs) were recorded by a commercialized PLQY measurement system from Ocean Optics with excitation from a 365-nm LED.

Computational methods

All calculations were carried out using the Vienna *ab initio* simulation package (VASP) with projector augmented wave (PAW) potentials [26,27]. DFT calculation was performed at a single point at the generalized gradient approximation of Perdew-Burke-Ernzerhof (GGA-PBE) [28]. The structure relaxations were carried out with a 450 eV plane-wave cutoff. The self-consistent total-energy difference and the convergence criterion for the forces on the atoms were set to 10^{-4} eV and 0.05 eV $Å^{-1}$, respectively. For *k*-point integration within the first Brillouin zone, 6×6×2 Monkhorst-Pack grid for $(C_4H_9NH_3)_2PbCl_4$ was selected. Based on the static states mentioned above, we calculated the corresponding band structures, density of states (DOSs) and formation energy for both undoped and Mn doped $(C_4H_9NH_3)_2PbCl_4$. In band structures and DOSs, the zero energy point was set to the Fermi level of the pure $(C_4H_9NH_3)_2PbCl_4$. The Mn-doped materials were corrected by aligning the electrostatic potential (V_{av}) of C atoms located far from the defects to the V_{av} for the same element in the pure $(C_4H_9NH_3)_2PbCl_4$ [29].

RESULTS AND DISCUSSION

As illustrated in Fig. 1a–c, a typical experiment for synthesizing the 2D perovskites consists of three steps: precursor synthesis (Fig. 1a), self-assembly (Fig. 1b) and crystallization (Fig. 1c). The crystallinity of the product is affected by the purity of precursor and crystallization time, and especially the toluene content plays a key role in the crystal quality of the sample. In addition, the synthesis results are repeatable. The PXRD patterns reflect only the

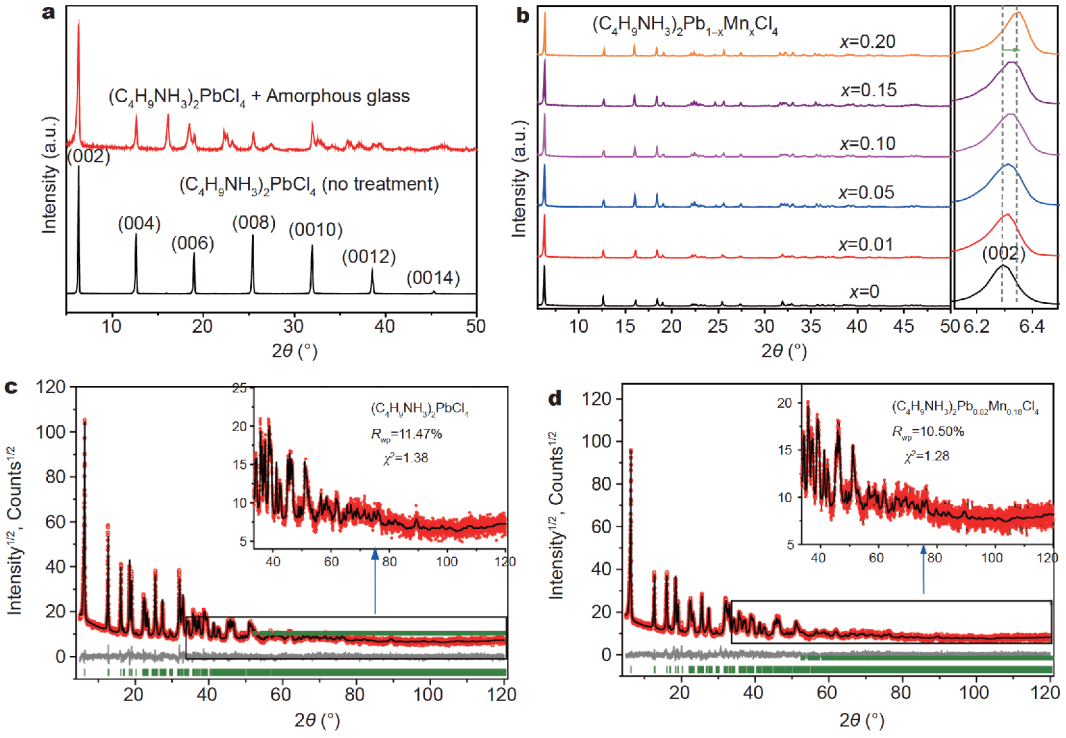

Figure 2 (a) The diffraction peaks on the (00*L*) crystallographic planes exist in the samples without treatment, which resulted from the preferred orientations. By adding a certain amount of amorphous glass, the preferred orientations were successfully eliminated. (b) PXRD patterns of the $(C_4H_9NH_3)_2Pb_{1-x}Mn_xCl_4$ samples with different Mn^{2+} doping concentrations, and the characteristic peaks of (002) planes which systemically shift to higher angles as Mn content increases. (c, d) The refined data are dependable by the qualified R_{wp} and χ^2 factors, showing that $(C_4H_9NH_3)_2PbCl_4$ belongs to the layered perovskite and Mn^{2+} occupies the Pb^{2+} sites.

diffraction peaks of (00*L*) (*L*=2, 4, 6, 8, 10, 12 and 14) crystal planes due to distinct preferred orientation, as shown in Fig. 2a, which also reveals the layered structure [14,15].

The preferred orientations were eliminated by the introduction of amorphous glass. The diffraction peaks of all crystallographic planes were obtained, which indicates that we have the opportunity to obtain the structural information by Rietveld refinement. The refinement results (Fig. 2c) reveal that $(C_4H_9NH_3)_2PbCl_4$ belongs to the orthorhombic system with a polar space group of *Pbca* at RT (Table 1). $(C_4H_9NH_3)_2PbCl_4$ adopts the 2D perovskite structure (Fig. 1d). Structurally, the alternating stacking of organic chain molecules and inorganic functional groups which are linked together by hydrogen bonds induces the formation of 2D layered perovskite structure. Due to the presence of organic molecules, mixed perovskite materials have more opportunities to achieve mechanical and structural modifications [30,31]. Accordingly, we tried to gain some attractive phenomena or characteristics through routine mechanochemical synthesis, such as grinding, heating and irradiation.

Table 1 Main parameters of refinement of the two samples of $(C_4H_9NH_3)_2PbCl_4$ and $(C_4H_9NH_3)_2Pb_{0.8}Mn_{0.2}Cl_4$

Compounds	$(C_4H_9NH_3)_2Pb_{1-x}Mn_xCl_4$	
x (%)	0	20
Sp.Gr.	*Pbca*	*Pbca*
a (Å)	7.989 (1)	7.989 (2)
b (Å)	7.860 (1)	7.882 (2)
c (Å)	27.979 (4)	27.825 (6)
V (Å^3)	1,756.8 (4)	1,752.0 (6)
Z	4	4
2θ-interval (°)	5–120	5–120
R_{wp} (%)	11.47	10.50
R_p (%)	8.68	7.87
χ^2	1.38	1.28
RB (%)	2.22	2.16

Herein, as shown in Fig. 1e, a designed amount of $MnBr_2$ was added to the perovskite crystals and then ground at RT. It is incredible that the sample rapidly exhibited orange-red fluorescence with continuous grinding when it was irradiated by an ultraviolet lamp

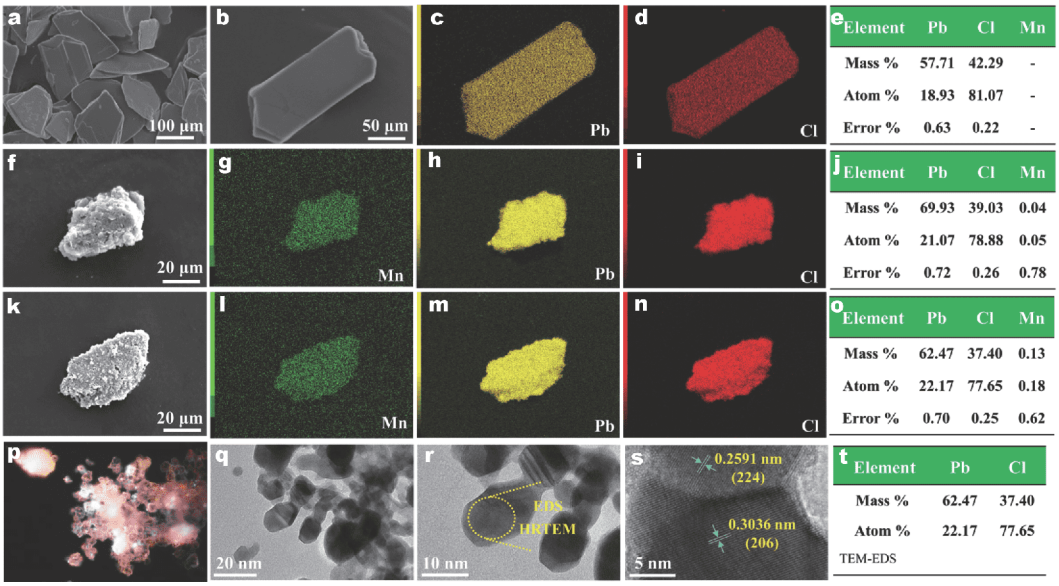

Figure 3 (a, b, f, k) Typical SEM images showing the layered morphology of $(C_4H_9NH_3)_2PbCl_4$ crystals (a, b), and the agglomeration states after grinding for $(C_4H_9NH_3)_2Pb_{0.95}Mn_{0.05}Cl_4$ (f) and $(C_4H_9NH_3)_2Pb_{0.8}Mn_{0.2}Cl_4$ (k). (c, d, g–i, l–n) Elemental mapping images demonstrate the homogeneous distribution of Pb, Cl and Mn in different samples. (e, j, o, t) listed the EDS results consistent with the chemical constituents of samples $(C_4H_9NH_3)_2PbCl_4$, $(C_4H_9NH_3)_2Pb_{0.95}Mn_{0.05}Cl_4$ and $(C_4H_9NH_3)_2Pb_{0.8}Mn_{0.2}Cl_4$. (p) Optical microscopy photograph of $(C_4H_9NH_3)_2Pb_{0.8}Mn_{0.2}Cl_4$ microcrystal particles with 365 nm UV excitation. (q, r) TEM images showing the layered perovskite sample $(C_4H_9NH_3)_2PbCl_4$ after grinding with nanoscale size; (s) HRTEM image of (224) and (206) crystallographic planes of $(C_4H_9NH_3)_2PbCl_4$ crystals.

with the emission wavelength of 365 nm. According to the DFT calculation, the crystal formation energy of $MnBr_2$ and $MnCl_2$ is −2.531 and −3.396 eV, respectively, indicating that high energy is needed to destroy $MnCl_2$. Therefore, $MnBr_2$ is a proper dopant source of Mn^{2+}.

It is well known that the mechanochemical synthesis lies not only in fundamental research but also in potential applications such as smart sensors, fluorescent biomarkers and deformation detectors. In this work, it is essential to unravel the nature of this phenomenon of mechanochemical synthesis 2D layered perovskite in depth. Benefitting from PXRD refinement, the crystallographic information of perovskite $(C_4H_9NH_3)_2Pb_{1-x}Mn_xCl_4$ can be obtained after sufficient grinding, thereby confirming the incorporation of Mn^{2+} ions. As shown in Fig. 2d, taking the crystal structure of $(C_4H_9NH_3)_2PbCl_4$ as the starting model, the Pb/Mn ratio in the sample x=0.2 was refined taking into account linear restriction *occ* (Pb) + *occ* (Mn) = 1. As we expected, the smaller cell volume of Mn-doped sample in comparison with that of host material is in a good agreement with smaller ion radii (IR) of Mn^{2+} (CN=6, 0.67–0.83 Å) than Pb^{2+} (CN=6, 1.19 Å). The average bond length $d(Pb–Cl)_{aver}$ (Table S2) also decreases with increasing Mn doping concentration. Chemical formula from refinements were $(C_4H_9NH_3)_2PbCl_4$ and $(C_4H_9NH_3)_2Pb_{0.82(1)}Mn_{0.18(1)}Cl_4$ which clearly showed that the Mn^{2+} ions entered the Pb^{2+} sites after grinding. Moreover, the synthesis of $(C_4H_9NH_3)_2Pb_{0.5}Mn_{0.5}Cl_4$ with high Mn^{2+} doping concentration was also performed. As shown in Fig. S1, the diffraction peaks of $PbBr_2$ appear in the PXRD pattern of $(C_4H_9NH_3)_2Pb_{0.5}Mn_{0.5}Cl_4$ at the high doping concentration of manganese. $PbBr_2$ can form relatively strong chemical bonds along with the substitution of Mn^{2+} for Pb^{2+} in the $(C_4H_9NH_3)_2PbCl_4$, without the substitution of Br^- into the $(C_4H_9NH_3)_2PbCl_4$ lattice.

In addition, Fig. 3a, b show the SEM images of $(C_4H_9NH_3)_2PbCl_4$ crystal with the largest particle size up to 100 μm. Fig. 3f, k present the morphology of the samples after grinding, showing that the particles agglomerate. Moreover, the composition uniformity of $(C_4H_9NH_3)_2Pb_{1-x}Mn_xCl_4$ was checked by elemental mapping. As shown in Fig. 3c, d, g–i and l–n, the manganese element is homogeneously distributed in these doped samples. Moreover, surface accumulation or phase segregation is not found. The average atomic ratios of Pb/Cl determined by EDS (Fig. 3e, j and o) are in accordance with that in the molecular formula 1:4. This further demonstrates that we developed an effective facile approach for incorporating Mn^{2+} into 2D organic-inorganic hybrid perovskite. Fig. 3p gives the optical microscopy photograph of $(C_4H_9NH_3)_2Pb_{0.98}Mn_{0.02}Cl_4$

with 365 nm UV light source excitation and exhibits the excellent luminescence properties which will be further discussed later.

To further demonstrate the morphology and structure evolution of $(C_4H_9NH_3)_2PbCl_4$, the TEM and the high resolution TEM (HRTEM) imaging were carried out, as shown in Fig. 3q–s. The size of the as-ground $(C_4H_9NH_3)_2PbCl_4$ was determined to be about 15 to 20 nm, indicating that 2D perovskite can be easily ground into nanoparticles. The solid diffusion reaction is mainly controlled by grain boundary diffusion, and the diffusion rate would be fast in nanoscale particles [32,33]. Meanwhile, the powder diffraction results (Fig. 2c, d) show that the crystal structure of the ground sample still belongs to 2D layered perovskite. The HRTEM results reveal lattice fringes with the planar spacing of 0.2591 and 0.3036 nm that corresponds to the (224) and (206) lattice planes of $(C_4H_9NH_3)_2PbCl_4$, respectively. As shown in Fig. 3t, we comparatively measured the chemical composition of Pb and Cl by TEM equipped with a windowless link EDS analyzer, consistent with the chemical ratio in the formula of $(C_4H_9NH_3)_2PbCl_4$.

To clarify the mechanism for Mn incorporation into the Pb site as observed experimentally, we performed the DFT calculations to obtain impurity formation energy of Mn^{2+} ions at the host $(C_4H_9NH_3)_2PbCl_4$. We have constructed a 4×4×1 supercell model for the layered perovskite crystal, based on the results of Rietveld refinement for the PXRD patterns of $(C_4H_9NH_3)_2PbCl_4$. Furthmore, the impurity formation energy (E_f) of a particular substitutional dopant is given by E_f=E(doped)-E(pure)+μ_{Pb}-μ_{Mn} (1), where E(doped) and E(pure) are the total energies of Mn-doped $(C_4H_9NH_3)_2Pb_{1-x}Mn_xCl_4$ and pristine $(C_4H_9NH_3)_2PbCl_4$, respectively. The chemical potentials μ_{Mn} and μ_{Pb} are those of the substitutional Mn and Pb, respectively [34].

The calculated results are summarized in Table 2, and the formation energy E_f (eV) of $(C_4H_9NH_3)_2Pb_{0.82}Mn_{0.18}Cl_4$ is −3.22 eV, indicating that the doped compound is easy to form and more stable than the pure one. Therefore, Mn^{2+} can enter the Pb sites at RT. This can also be a reasonable explanation for the above phenomenon, that is, the luminescent features can be rapidly changed only by room-temperature grinding in Mn^{II}-based 2D hybrid perovskite.

Then, we systematically studied the optical properties of $(C_4H_9NH_3)_2Pb_{1-x}Mn_xCl_4$. As can be seen from the normalized absorption and emission spectra in Fig. 4a, the $(C_4H_9NH_3)_2Pb_{1-x}Mn_xCl_4$ (x>0) samples exhibit a narrow emission and a broad emission band peaking at

Table 2 Total energies (eV) of $(C_4H_9NH_3)_2PbCl_4$ and $(C_4H_9NH_3)_2Pb_{0.82}Mn_{0.18}Cl_4$. The chemical potentials (eV) of Mn and Pb

Models	Total energy (eV)
$(C_4H_9NH_3)_2PbCl_4$	−788.77
$(C_4H_9NH_3)_2Pb_{0.82}Mn_{0.18}Cl_4$	−793.941
	Chemical potential (eV)
Mn	−9.076
Pb	−7.124

~405 and ~615 nm at the exciting wavelength of 365 nm. Meanwhile, the ratio of the narrow emission to the broad emission decreases with increasing Mn^{2+} content and the corresponding Commission Internationale de L'Eclairage (CIE) chromaticity diagrams calculated from the emission spectra of samples are shown in Fig. 4b. Especially, as shown in Fig. S3a, b, the pure $(C_4H_9NH_3)_2PbCl_4$ has trap emissions in the wavelength region of 450–650 nm and 755–785 nm. And the fluorescence intensity is very weak due to a large number of defects. The trap emissions almost disappeared with the incorporation of Mn^{2+}. Simultaneously, as shown in Fig. 4c, the band-edge emission spectrum of the host $(C_4H_9NH_3)_2Pb_{1-x}Mn_xCl_4$ overlaps with one side of the excitation spectrum of Mn^{2+}, proposing that the samples have the possibility of energy transfer. Herein, to determine if the energy transfer between Mn^{2+} and the host is responsible for the light emission, the luminescence decays were monitored at λ_{em}=405 and 615 nm. The fluorescence decays of band gap transition and Mn^{2+} $^4T_1 \rightarrow {}^6A_1$ transition under 365 nm excitation as a function of the Mn^{2+} doping concentration in $(C_4H_9NH_3)_2Pb_{1-x}Mn_xCl_4$ (x=0.01–0.20) are exhibited in Fig. 4d and e.

A double exponential decay process was observed with different x in $(C_4H_9NH_3)_2Pb_{1-x}Mn_xCl_4$ (x=0.01–0.20), and the curves were well fitted by $I=A_1\exp(-t/\tau_1)+A_2\exp(-t/\tau_2)$ [35], where I is the luminescence intensity, t is the time after excitation, τ_i (i=1,2) represents the decay time of i component, and parameters A_1 and A_2 are the fitting constants. Moreover, the average lifetime (τ) can be determined using the calculation below: $\tau=(A_1\tau_1^2+A_2\tau_2^2)/(A_1\tau_1+A_2\tau_2)$ [34,35].

As shown in Fig. 4f, the lifetime of band gap transition decreases continuously with the increase of Mn^{2+} concentration. The lifetime decreases to 4.682 ns at x=0.20 compared with that at x=0.01 (5.448 ns), suggesting the energy transfer exists between the host and Mn^{2+} [14,36–38]. It is confused to explain that the lifetime of Mn^{2+} decreases with the increase of Mn^{2+} concentration. We may attribute this to concentration

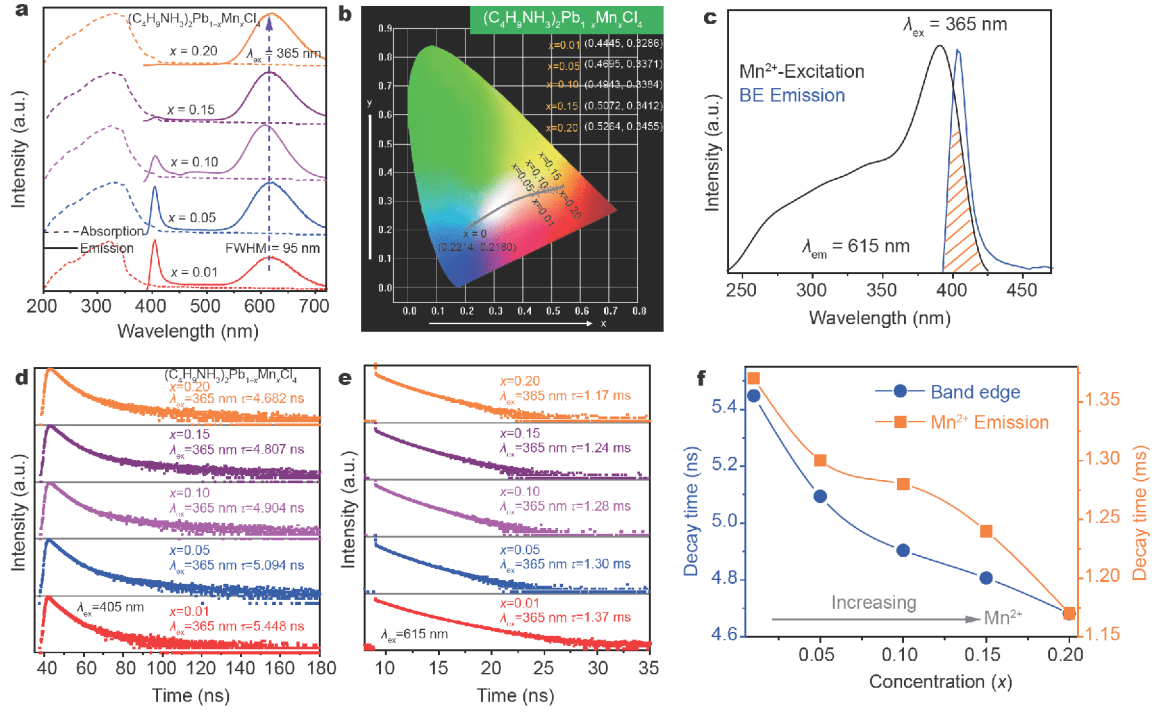

Figure 4 Optical properties of the samples. (a) Normalized absorption and PL spectra of $(C_4H_9NH_3)_2Pb_{1-x}Mn_xCl_4$ (x>0) with varying Mn^{2+} contents. The band-edge emission intensity of the host decreases with increasing Mn^{2+} content, while the orange Mn^{2+} emission increases with increasing dopant concentration. (b) CIE coordinates of $(C_4H_9NH_3)_2Pb_{1-x}Mn_xCl_4$. (c) The excitation spectrum of Mn^{2+} (λ_{em}=615 nm) and the emission spectrum of the host (λ_{ex}=365 nm) at the same coordinate system. PL decay curves of corresponding $(C_4H_9NH_3)_2Pb_{1-x}Mn_xCl_4$ (x>0) samples recorded at λ_{ex}=365 nm, (d) λ_{em}=405 nm and (e) λ_{em}=615 nm. (f) Dependence of the lifetime on different Mn^{2+}-doping concentration.

quenching. The efficient energy transfer from excitons to Mn^{2+} relies on the exchange coupling of dipoles, similar to the case of Mn-doped halogenation perovskite quantum dots [22]. Especially, we conjecture that the peak at 405 nm is due to band-edge emission which originates from band gap transition of the host itself. The orange-red emission at 615 nm results from an internal $^4T_1$ to $^6A_1$ transition of the Mn^{2+} dopants excited by energy transfer from the host $(C_4H_9NH_3)_2Pb_{1-x}Mn_xCl_4$. In addition, the PLQYs of the $(C_4H_9NH_3)_2Pb_{1-x}Mn_xCl_4$. ($x$=0.01, 0.05, 0.10, 0.15, 0.20) were measured upon 365 nm excitation, and the corresponding values are 15.5%, 16.2%, 16.8%, 19.4%, 27.9%.

The absorption spectra of $(C_4H_9NH_3)_2Pb_{1-x}Mn_xCl_4$ are shown in Fig. S2a–f. The exciton absorption peaks are observed at the absorption edge in 2D hybrid perovskites [39,40]. Considering the exciton absorption, the optical band gaps of $(C_4H_9NH_3)_2Pb_{1-x}Mn_xCl_4$ (x=0, 0.01, 0.05, 0.10, 0.15, 0.20) are calculated to be about 3.51, 3.46, 3.41, 3.36, 3.32, and 3.30 eV (see the detail in the Supplementary information). Additionally, the electronic band structures and DOS of $(C_4H_9NH_3)_2PbCl_4$ and $(C_4H_9NH_3)_2Pb_{0.8}Mn_{0.2}Cl_4$ calculated with DFT are illustrated in Fig. 5a–d. The structural models used for the calculation are based on the PXRD refinement. The calculations predict a directed band gap (E_g) of 3.12 eV, with the conduction band minimum (CBM) and valence band maximum both located at the k-point of U. When Mn doping concentration is 20%, the band gap decreases to 3.07 eV. Fig. 5c displays the calculated total and partial DOSs of $(C_4H_9NH_3)_2PbCl_4$, indicating that the top of the valence band is dominated by the orbitals of Cl while the CBM are mainly constituted by the orbitals of Pb. After Mn^{2+} incorporation, localized energy levels from Mn^{2+} appear above the valence band and just at the CBM as shown in Fig. 5d, which induces the possible additional transition. Since the energy level of Mn is located just at the CBM, photo-generated electrons in the semiconductor could easily jump from the CBM to Mn. This process together with the energy transfer mentioned above causes the efficient luminescence of Mn^{2+}. Fig. 5e illustrates the schematic process of Mn^{2+} entering the crystal lattice of 2D layered perovskite $(C_4H_9NH_3)_2Pb_{1-x}Mn_xCl_4$, and the schematic luminescence process in $(C_4H_9NH_3)_2Pb_{1-x}$-

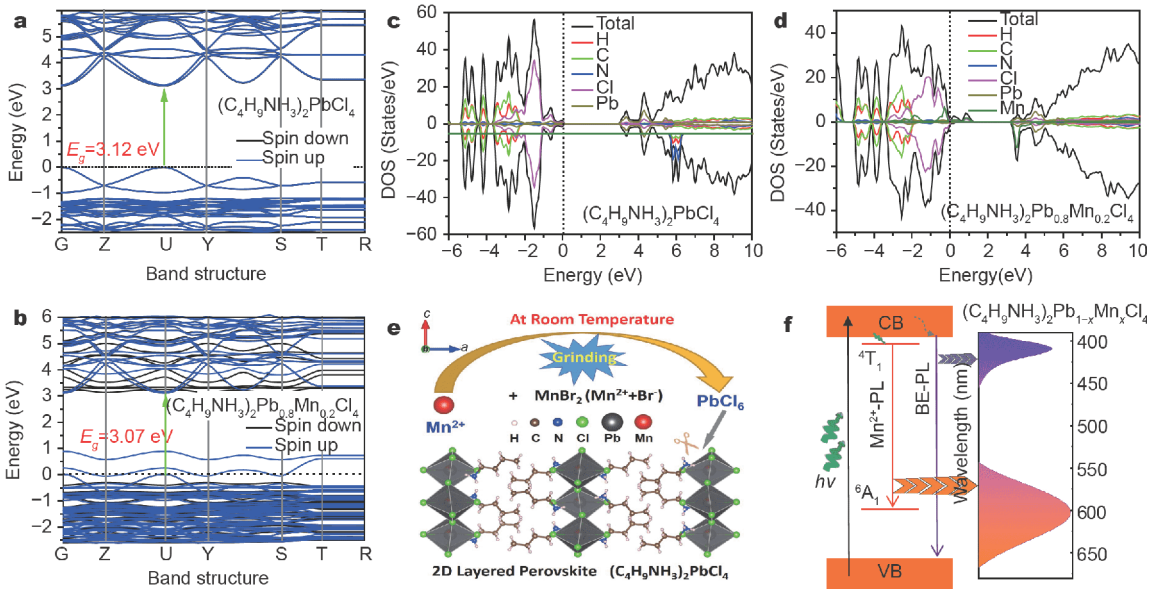

Figure 5 (a, b) Electronic band structures, (c, d) partial density of states of $(C_4H_9NH_3)_2PbCl_4$ and $(C_4H_9NH_3)_2Pb_{0.8}Mn_{0.2}Cl_4$ suggesting that the 2D layered hybrid perovskite $(C_4H_9NH_3)_2PbCl_4$ belongs to a direct band gap semiconductor. (e) Experimental illustration of divalent manganese ions (Mn^{II}) entering 2D layered perovskite $(C_4H_9NH_3)_2PbCl_4$. (f) Schematic energy level diagram of Mn^{2+} doped $(C_4H_9NH_3)_2PbCl_4$ suggesting the unification of band-edge emission and Mn^{2+} doping luminescence from the energy transfer effect.

Mn_xCl_4 is described in Fig. 5f. Briefly, the violet and orange emissions of $(C_4H_9NH_3)_2Pb_{1-x}Mn_xCl_4$ are attributed to band-edge emission and Mn^{2+} transition from $^4T_1$ to $^6A_1$ due to an efficient energy transfer, respectively. The 615 nm orange-emitting $(C_4H_9NH_3)_2Pb_{1-x}Mn_xCl_4$ phosphor can be used in white light emitting diode (WLED) device with a commercially available 365 nm LED chip.

CONCLUSIONS

In summary, we obtained a lamellar 2D perovskite $(C_4H_9NH_3)_2PbCl_4$ crystal, and incorporated Mn^{2+} ions into the 2D structures by a facile mechanochemical synthesis approach with grinding the mixtures at RT. The structure refinement suggests that Mn^{2+} ions occupy the Pb^{2+} sites in $(C_4H_9NH_3)_2Pb_{1-x}Mn_xCl_4$. The negative formation energy (−3.22 eV) indicated that the Mn^{2+} ions can enter the lattice rapidly through molecular diffusion in ambient atmosphere due to the unique crystalline structure of the 2D hybrid perovskite. The fluorescence of $(C_4H_9NH_3)_2Pb_{1-x}Mn_xCl_4$, corresponding to emissions at 405 and 615 nm, is attributed to $(C_4H_9NH_3)_2PbCl_4$ band-edge emission and Mn^{2+} $^4T_1 \rightarrow {}^6A_1$ transition due to an efficient energy transfer. This work opens up new possibilities to design and prepare complicated or doped 2D hybrid perovskites with the aid of the unqiue exchange strategy between cations which could be used for emerging opotoelectronic applicaions.

Received 16 December 2018; accepted 12 February 2019; published online 4 March 2019

1 Tian Y, Zhou C, Worku M, *et al.* Highly efficient spectrally stable red perovskite light-emitting diodes. Adv Mater, 2018, 30: 1707093
2 Stoumpos CC, Cao DH, Clark DJ, *et al.* Ruddlesden–popper hybrid lead iodide perovskite 2D homologous semiconductors. Chem Mater, 2016, 28: 2852–2867
3 Qin X, Dong H, Hu W. Green light-emitting diode from bromine based organic-inorganic halide perovskite. Sci China Mater, 2015, 58: 186–191
4 Ma S, Cai M, Cheng T, *et al.* Two-dimensional organic-inorganic hybrid perovskite: From material properties to device applications. Sci China Mater, 2018, 61: 1257–1277
5 Mao L, Ke W, Pedesseau L, *et al.* Hybrid Dion–Jacobson 2D lead iodide perovskites. J Am Chem Soc, 2018, 140: 3775–3783
6 Pathak S, Sakai N, Wisnivesky Rocca Rivarola F, *et al.* Perovskite crystals for tunable white light emission. Chem Mater, 2015, 27: 8066–8075
7 Tan Z, Wu Y, Hong H, *et al.* Two-dimensional $(C_4H_9NH_3)_2PbBr_4$ perovskite crystals for high-performance photodetector. J Am Chem Soc, 2016, 138: 16612–16615
8 Dou L, Wong AB, Yu Y, *et al.* Atomically thin two-dimensional organic-inorganic hybrid perovskites. Science, 2015, 349: 1518–1521
9 Hu H, Meier F, Zhao D, *et al.* Efficient room-temperature phosphorescence from organic-inorganic hybrid perovskites by molecular engineering. Adv Mater, 2018, 30: 1707621
10 Li L, Sun Z, Wang P, *et al.* Tailored engineering of an unusual

$(C_4H_9NH_3)_2(CH_3NH_3)_2Pb_3Br_{10}$ two-dimensional multilayered perovskite ferroelectric for a high-performance photodetector. Angew Chem Int Ed, 2017, 56: 12150–12154
11 Cao DH, Stoumpos CC, Farha OK, *et al.* 2D homologous perovskites as light-absorbing materials for solar cell applications. J Am Chem Soc, 2015, 137: 7843–7850
12 Mao L, Wu Y, Stoumpos CC, *et al.* Tunable white-light emission in single-cation-templated three-layered 2D perovskites $(CH_3CH_2NH_3)_4Pb_3Br_{10-x}Cl_x$. J Am Chem Soc, 2017, 139: 11956–11963
13 Dohner ER, Jaffe A, Bradshaw LR, *et al.* Intrinsic white-light emission from layered hybrid perovskites. J Am Chem Soc, 2014, 136: 13154–13157
14 Biswas A, Bakthavatsalam R, Kundu J. Efficient exciton to dopant energy transfer in Mn^{2+}-doped $(C_4H_9NH_3)_2PbBr_4$ two-dimensional (2D) layered perovskites. Chem Mater, 2017, 29: 7816–7825
15 Amerling E, Baniya S, Lafalce E, *et al.* Electroabsorption spectroscopy studies of $(C_4H_9NH_3)_2PbI_4$ organic–inorganic hybrid perovskite multiple quantum wells. J Phys Chem Lett, 2017, 8: 4557–4564
16 Lu YB, Guan CB, sun H, *et al.* Investigation on enhanced moisture resistance of two-dimensional layered hybrid organic–inorganic perovskites $(C_4H_9NH_3)_2PbI_4$. J Phys Chem C, 2018, 122: 11862–11869
17 Yangui A, Garrot D, Lauret JS, *et al.* Optical investigation of broadband white-light emission in self-assembled organic-inorganic perovskite $(C_6H_{11}NH_3)_2PbBr_4$. J Phys Chem C, 2015, 119: 23638–23647
18 Li YY, Lin CK, Zheng GL, *et al.* Novel <110>-oriented organic −inorganic perovskite compound stabilized by *N*-(3-aminopropyl) imidazole with improved optical properties. Chem Mater, 2006, 18: 3463–3469
19 Dohner ER, Hoke ET, Karunadasa HI. Self-assembly of broadband white-light emitters. J Am Chem Soc, 2014, 136: 1718–1721
20 Xu K, Lin CC, Xie X, *et al.* Efficient and stable luminescence from Mn^{2+} in core and core–isocrystalline shell $CsPbCl_3$ perovskite nanocrystals. Chem Mater, 2017, 29: 4265–4272
21 Guria AK, Dutta SK, Adhikari SD, *et al.* Doping Mn^{2+} in lead halide perovskite nanocrystals: successes and challenges. ACS Energy Lett, 2017, 2: 1014–1021
22 Liu W, Lin Q, Li H, *et al.* Mn^{2+}-doped lead halide perovskite nanocrystals with dual-color emission controlled by halide content. J Am Chem Soc, 2016, 138: 14954–14961
23 Yan D, Gao R, Wei M, *et al.* Mechanochemical synthesis of a fluorenone-based metal organic framework with polarized fluorescence: an experimental and computational study. J Mater Chem C, 2013, 1: 997–1004
24 James SL, Adams CJ, Bolm C, *et al.* Mechanochemistry: Opportunities for new and cleaner synthesis. Chem Soc Rev, 2012, 41: 413–447
25 Heintz A , Fink M , Mitchell B . Mechanochemical synthesis of blue luminescent alkyl/alkenyl-passivated silicon nanoparticles. Adv Mater, 2007, 19: 3984–3988
26 Kresse G, Furthmüller J. Efficient iterative schemes for *ab initio* total-energy calculations using a plane-wave basis set. Phys Rev B, 1996, 54: 11169–11186
27 Kresse G, Joubert D. From ultrasoft pseudopotentials to the projector augmented-wave method. Phys Rev B, 1999, 59: 1758–1775
28 Perdew JP, Burke K, Ernzerhof M. Generalized gradient approximation made simple. Phys Rev Lett, 1996, 77: 3865–3868
29 Zhang J, Dang W, Ao Z, *et al.* Band gap narrowing in nitrogen-doped $La_2Ti_2O_7$ predicted by density-functional theory calculations. Phys Chem Chem Phys, 2015, 17: 8994–9000
30 Liu Y, Yao D, Zhang H. Self-assembly driven aggregation-induced emission of copper nanoclusters: a novel technology for lighting. ACS Appl Mater Interfaces, 2017, 10: 12071–12080
31 Huitorel B, El Moll H, Cordier M, *et al.* Luminescence mechanochromism induced by cluster isomerization. Inorg Chem, 2017, 56: 12379–12388
32 Goodner MD, DeSimone JM, Kiserow DJ, *et al.* An equilibrium model for diffusion-limited solid-state polycondensation. Ind Eng Chem Res, 2000, 39: 2797–2806
33 Haerifar M, Azizian S. Mixed surface reaction and diffusion-controlled kinetic model for adsorption at the solid/solution interface. J Phys Chem C, 2013, 117: 8310–8317
34 Guo S, Wang Y, Wang C, *et al.* Large spin-orbit splitting in the conduction band of halogen (F, Cl, Br, and I) doped monolayer WS_2 with spin-orbit coupling. Phys Rev B, 2017, 96: 245305
35 Huang CH, Chen TM, Liu WR, *et al.* A single-phased emission-tunable phosphor $Ca_9Y(PO_4)_7:Eu^{2+},Mn^{2+}$ with efficient energy transfer for white-light-emitting diodes. ACS Appl Mater Interfaces, 2010, 2: 259–264
36 Fei L, Yuan X, Hua J, *et al.* Enhanced luminescence and energy transfer in Mn^{2+} doped $CsPbCl_{3-x}Br_x$ perovskite nanocrystals. Nanoscale, 2018, 10: 19435–19442
37 Li F, Xia Z, Pan C, *et al.* High Br^- content $CsPb(Cl_yBr_{1-y})_3$ perovskite nanocrystals with strong Mn^{2+} emission through diverse cation/anion exchange engineering. ACS Appl Mater Interfaces, 2018, 10: 11739–11746
38 Parobek D, Roman BJ, Dong Y, *et al.* Exciton-to-dopant energy transfer in Mn-doped cesium lead halide perovskite nanocrystals. Nano Lett, 2016, 16: 7376–7380
39 Stoumpos CC, Soe CMM, Tsai H, *et al.* High members of the 2D Ruddlesden-Popper halide perovskites: synthesis, optical properties, and solar cells of $(CH_3(CH_2)_3NH_3)_2(CH_3NH_3)_4Pb_5I_{16}$. Chem, 2017, 2: 427–440
40 Li J, Luo L, Huang H, *et al.* 2D behaviors of excitons in cesium lead halide perovskite nanoplatelets. J Phys Chem Lett, 2017, 8: 1161–1168

Acknowledgements The present work was supported by the National Natural Science Foundation of China (91622125, 51722202 and 51572023) and the Natural Science Foundation of Beijing (2172036), and Molokeev M acknowledges the support of the Russian Foundation for Basic Research (17-52-53031). The DFT calculation was carried out at the National Supercomputer Center in Tianjin, and the calculations were performed on TianHe-1(A).

Author contributions Xia Z conceived the idea and designed the experiments. Zhang J and Guo S engineered the theoretical calculation. Zhou G performed the material synthesis, measurements and prepared the manuscript with support from Zhao J, Xia Z and Liu Q. Molokeev M performed the structure refinement. All authors contributed to the general discussion.

Conflict of interest The authors declare no conflict of interest.

Supplementary information Supplementary information is available in the online version of this article.

Guojun Zhou is a PhD student in the University of Science and Technology Beijing under the supervision of Prof. Zhiguo Xia. He completed his bachelor degree (applied physics) from Taiyuan Normal University in 2014 and received the master degree from China University of Geosciences, Beijing in 2017. His research mainly focuses on the structural design and luminescence properties of two-dimensional organic-inorganic hybrid perovskite.

Junying Zhang is a professor in the School of Physics, Beihang University. She received her BSc degree (1996) and master degree (1999) from the University of Science and Technology Beijing, and PhD degree (2002) from Tsinghua University. She joined Beihang University in 2002 and became a full professor in 2009. She conducted research as an academic visitor in the University of Oxford in 2015. Her research interest focuses on photo-functional materials including broad-spectrum solar light photocatalysts, nano-size luminescence materials, and few-layer/monolayer materials and devices.

Zhiguo Xia is a professor of materials chemistry and physics in the University of Science and Technology Beijing (USTB). He obtained his bachelor degree in 2002 and master degree in 2005 from Beijing Technology and Business University, and he received his PhD degree from Tsinghua University in 2008. His research interest includes two parts, and one is about the discovery of the new rare earth doped solid state materials, and the other one is the discovery of the new luminescent perovskite crystals, nanocrystals and their luminescence properties.

Mn^{II}掺杂二维杂化钙钛矿$(C_4H_9NH_3)_2PbCl_4$的机械化学合成及其发光性能研究

周国君[1], 郭少强[2], 赵静[1], Maxim Molokeev[3,4,5], 刘泉林[1], 张俊英[2*], 夏志国[1*]

摘要 简单和高效的机械力化学合成方法在先进功能材料的合成领域备受关注. 本论文通过机械力化学合成手段, 将二价锰离子(Mn^{II})成功掺杂于二维层状钙钛矿$(C_4H_9NH_3)_2PbCl_4$中. 研究发现, 仅通过室温研磨便能观察到二维杂化钙钛矿中, 迅速出现Mn^{II}的橙红色荧光. 其中, 掺杂的Mn^{II}占据了Pb的格位, 其荧光特性源于$(C_4H_9NH_3)_2Pb_{1-x}Mn_xCl_4$的带边发射和$Mn^{II}$的$^4T_1\rightarrow{}^6A_1$跃迁之间的能量传递; 与此同时, 利用第一性原理计算了钙钛矿$(C_4H_9NH_3)_2Pb_{1-x}Mn_xCl_4$掺杂前后的形成能, 从理论上证明了具有特殊结构的二维杂化钙钛矿使得Mn^{2+}易于替代Pb^{2+}. 鉴于机械化学合成方法在二维层状钙钛矿中不仅易掺杂且光谱可调的优势, 将为新材料领域的进一步开发和应用提供新的机遇.